Near-Surface Geophysical Imaging of a Talus Deposit in Yosemite Valley, California

ANNA G. BRODY

CHRISTOPHER J. PLUHAR[1]

Department of Earth and Environmental Sciences, California State University, Fresno, 2576 East San Ramon Avenue, Mail Stop ST-24, Fresno, CA 93740

GREG M. STOCK

National Park Service, Yosemite National Park, 5083 Foresta Road Box 700, El Portal, CA 95389

W. JASON GREENWOOD

Advanced Geosciences, Inc., 2121 Geoscience Drive, Austin, TX 78726

Key Terms: ***Geophysics, Ground Penetrating Radar, Seismic Refraction, Electrical Resistivity, Mass Wasting, Rock Fall***

ABSTRACT

Talus at the base of cliffs in Yosemite Valley, CA, represents rock fall and debris avalanche accumulation occurring since the glacial retreat after the last glacial maximum. This ongoing mass wasting subjects humans and infrastructure to hazards and risk. In order to quantify post-glacial rock-fall rates, talus volumes are needed for the deposits of interest. We used three near-surface geophysical methods (ground penetrating radar, electrical resistivity, and seismic refraction) to locate the basal contact of talus below Glacier Point, near Curry Village in the eastern Yosemite Valley. The coarseness of the talus deposit limited our ability to use these methods in some areas, and the geometry at the base of the cliff restricted our ability to conduct seismic refraction and electrical resistivity across the talus-bedrock boundary there. Nonetheless, we were able to detect the basal boundary of talus on top of both bedrock and glacio-fluvial sediment fill. Geophysical imaging revealed an apparent onlapping relationship of talus over aggrading post-glacial sediment fill, and our data support the proposition of approximately 5 m of valley floor aggradation since deglaciation. The bedrock-talus contact is characterized by a dip of 52–64°, consistent with the dip of the cliff surface above the talus apex. Ground penetrating radar and resistivity were the most diagnostic methods, in addition to being the most rapid and easiest to implement on this type of deposit.

INTRODUCTION

Yosemite Valley, located in the central Sierra Nevada of California (Figure 1), provides an outstanding natural laboratory for studying rock fall in isolation from the complicating influences of other mass wasting processes. The 1-km-tall sheer granitic walls of Yosemite Valley, sculpted by alpine glaciers during the Pleistocene and mostly devoid of soils, have subsequently been modified almost exclusively by rock-fall processes.

Rock falls present a threat to the approximately four million people that visit Yosemite National Park annually, as well as to infrastructure and facilities (Guzzetti et al., 2003; Stock et al., 2013). Between 1857 and 2011, 15 people were killed and at least 85 seriously injured by such events in Yosemite Valley (Stock et al., 2013). An inventory of historical rock falls in Yosemite (Stock et al., 2013) forms the basis for numerous studies of rock-fall–triggering mechanisms and volume-frequency relations (e.g., Wieczorek et al., 1995, 1999; Wieczorek and Jäger, 1996; Dussauge-Peisser et al., 2002; Dussauge et al., 2003; and Guzzetti et al., 2003). This historical inventory is valuable but suffers from variable reporting rates through time, incomplete reporting of small events, coarse estimates of rock-fall volumes for most catalogued events, and the relatively short duration of the observation record (155 years). As a result, measures of long-term (thousands of years) rock-fall activity are needed to evaluate historical activity, to

[1]Corresponding author email: cpluhar@csufresno.edu.

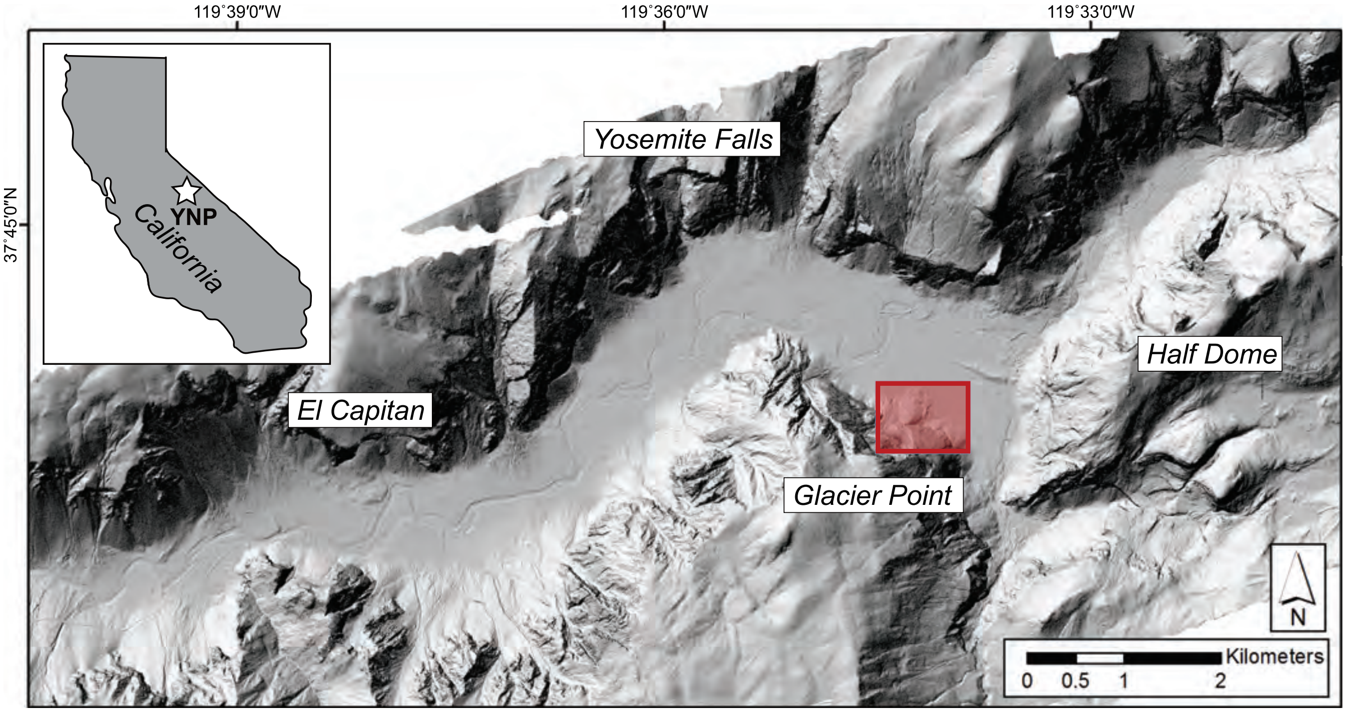

Figure 1. Location map of studied talus deposit in Yosemite Valley, Yosemite National Park (YNP), CA, shown in hillshade (illumination angle = 315°, azimuth = 45°) derived from a 1 × 1–m LiDAR-based digital elevation model. Red box indicates study area beneath Glacier Point shown in Figure 2.

examine the possibility of changes in rock-fall rate with time, and to examine geologically relevant volume-frequency distributions of rock fall.

The long-term record of rock-fall activity in Yosemite Valley is preserved in the rock-fall debris, or talus, that has accumulated beneath the valley walls. These deposits consist of volumes of many millions of cubic meters and reach heights of more than 100 m above the floor of Yosemite Valley. Because the floor of Yosemite Valley is wide (~1 km) and very low gradient (~3 m/km), there is very little post-depositional modification or degradation of talus slopes. Thus, the talus deposits in Yosemite Valley offer a unique opportunity to quantify long-term rock-fall activity (e.g., Wieczorek and Jäger, 1996). Critically, such quantification relies on assumptions about the state of the valley floor immediately following deglaciation. It is reasonable to presume that each major glacial advance down the valley removed accumulated talus from the previous interglacial period, such that the talus deposits record the accumulation since ice last retreated from the valley. If correct, the talus in Yosemite Valley would have accumulated for only the past 15,000–17,000 years, the approximate age of local glacial retreat at the end of the Last Glacial Maximum (LGM) (Huber, 1987; Wieczorek and Jäger, 1996; and Stock and Uhrhammer, 2010). Since deglaciation, sparse data suggest approximately 5 m of aggradation of the valley floor with glacio-fluvial sediments (Cordes et al., 2013).

In order to evaluate these presumptions, we employed near-surface geophysical imaging techniques to map the subsurface extent of a talus deposit in Yosemite Valley. Our research builds upon successful work in the European Alps using ground penetrating radar (GPR), seismic refraction (SR), and two-dimensional–resistivity (2DR) methods to define shallow subsurface (<30-m) contacts between bedrock and talus (e.g., Otto and Sass, 2006; Sass, 2006, 2007). Here we demonstrate that these methods can help constrain the subsurface extent of thick talus accumulations against both a steeply dipping bedrock contact and underlying glacio-fluvial sediments.

STUDY AREA

Geologic Setting of Yosemite Valley

Topographic relief in Yosemite Valley derives from creation of the Sierra Nevada batholith during Mesozoic Farallon–North America subduction and arc volcanism (Bateman, 1992), erosion during the Paleogene (Wakabayashi and Sawyer, 2001), and rejuvenation of relief since the mid-Miocene (e.g., Huber, 1981; Wakabayashi and Sawyer, 2001).

Multiple Quaternary glaciations deepened and modified the drainage network of the Sierra Nevada (Wahrhaftig and Birman, 1965; Huber, 1987). The most recent period of glaciation, locally called the Tioga glaciation, peaked between 28 and 17 ka (Bursik and Gillespie, 1993; Phillips et al., 2009), corresponding with the global LGM. Unlike previous glaciations, which filled Yosemite Valley to the rim, the Tioga glaciation only extended part way up the valley walls (Matthes, 1930; Huber, 1987; and Wieczorek et al., 2008). Matthes (1930) mapped the extent of the Tioga glaciation in Yosemite Valley, denoting the farthest advancement by the presence of a probable terminal moraine near Bridalveil Meadow. Deglaciation of the valley occurred beginning about 19,000 years before present (BP), with most of the valley free from ice by 15 ka (Smith and Anderson, 1992; Stock and Uhrhammer, 2010). Below the Tioga trimline, the steep cliffs were scoured by glacial erosion, with some cliffs still retaining glacial polish. In contrast, areas above the Tioga trimline are less steep and have been weathered for a much longer interval, promoting rock falls from those areas (Bronson and Watters, 1987; Wieczorek et al., 2000, 2008; and Guzzetti et al., 2003).

We chose the Curry Village talus cone for geological, hazard assessment, and survey feasibility reasons. The relatively simple talus accumulation here appears to consist entirely of blocks from fragmental-type rock falls (i.e., no large rock avalanches) and is also free from other possible modes of accumulation, such as debris slides or debris flows, ensuring that we understand the processes creating the deposit. In addition, it is located adjacent to areas in which something is known of the subsurface (Cordes et al., 2013; National Park Service, 2013). The project also contributes to hazard assessment of the populated Curry Village, with its history of damaging rock falls. This project permitted the quantification of geological rock-fall rates (Brody, 2011) for comparison to historical rates. Finally, the survey location represents one of only a few areas in Yosemite Valley where geophysical equipment could be deployed effectively. Many of the active talus cones consist entirely of cobbles to boulders, with little option for inserting electrical resistivity electrodes and Betsy Seisgun™ shots or coupling to GPR antennae.

Rock-fall source areas for talus deposits near Curry Village consist of the Half Dome Granodiorite and Granodiorite of Glacier Point (Peck, 2002). At Glacier Point, numerous joint sets (Wieczorek and Snyder, 1999; Weizorek et al., 2008; and Matasci et al., 2011) provide planes of weakness from which the rock falls of the study area often originate. The most prominent sets are nearly vertically oriented and moderately east-dipping regional-scale joints. The intersection of these dominant features with other joint sets is responsible for the overall structure of the cliffs at this location (Matasci et al., 2011). The most numerous joints present at Glacier Point are sheeting (exfoliation) joints that have formed subparallel to the topographic surface (Wieczorek and Snyder, 1999; Stock et al., 2011).

The studied talus deposit is located on the floor of Yosemite Valley east of Curry Village, beneath Glacier Point. In this area, the cliff below Glacier Point is a curving, glacially polished bedrock slab with a surface slope (dip) of approximately 60–65°, known locally as the Glacier Point Apron. Large deposits of talus flank the base of the Glacier Point Apron. These deposits are up to 130 m thick and extend as much as 370 m outward from the base of the cliff. Talus clast size at the study area increases with distance from the apex of the deposit as a result of "gravity sorting," characteristic of talus slopes formed by fragmental-type rock falls (Evans and Hungr, 1993). Sand- to cobble-sized debris dominates the upper several meters of the slope proximal to the cliff face, with larger boulders up to tens of cubic meters in volume on the distal portion of the slope. Although talus near Curry Village has accumulated since 15–17 ka, at least 28 historical rock falls and rock slides recorded from above Curry Village have contributed to the overall talus volume there (Figure 2; Stock et al., 2013). This includes several notable and well-documented rock falls since 1998, with volumes ranging from about 213 to 5,637 m^3 (Wieczorek and Snyder, 1999; Wieczorek et al., 2008; and Stock et al., 2011, 2013).

Geophysical Survey Line

To map the basal contact of the talus deposit, we employed geophysical techniques on a survey line positioned along the boundary between two talus cones near Curry Village (Figure 1, inset). We selected this location as a result of (1) the likelihood of imaging the basal contact of talus against crystalline bedrock and glacio-fluvial sediment fill in this relatively thinner portion of the talus deposit and (2) the ability to insert geophysical equipment into the finer-grained talus debris to the necessary depth (30–60 cm) below grade. The survey line originates at 1,262 m in elevation at the base of the Glacier Point Apron cliff face, extends north toward the valley floor along a strike of N68°E, and ends at 1,218 m in elevation beyond the distal edge of the talus. The surface slope averages approximately 12.5° along the profile line, with a maximum of about 17° in the upper portion near the cliff face. At the southern end

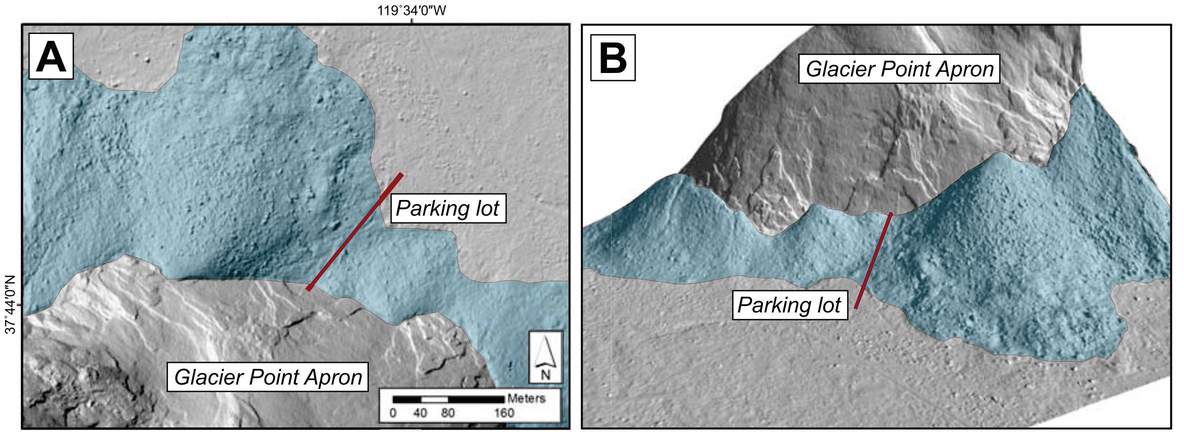

Figure 2. Talus deposits beneath Glacier Point Apron in eastern Yosemite Valley, shown in plan view (A) and oblique view (B) as viewed from the northeast. Areal extent of studied talus deposit shown in blue; geophysical survey line denoted by red line. The parking lot indicated caps a landfill site, the margin of which lies more than ten meters to the southeast of the geophysical profile line.

of the survey line, adjacent to the bedrock cliff, the deposit consists of sands, gravel, and cobbles (Figure 3A). Downslope from this, the upper section of the survey line is relatively steep and is composed primarily of gravel and cobble-sized clasts. Approximately halfway down the slope, a small seasonal stream traverses the profile line in two locations, demonstrating that the talus slope experiences minor modification by other processes (Figure 3B). The middle section of the survey line has a lower gradient and is dominated by gravel and cobbles, with numerous large boulders present (Figure 3C). The lower section of the profile exhibits a sandy texture and is crossed by the same stream present in the upper section of the survey line (Figure 3D). The survey line terminates west of a parking lot, beyond the approximate surficial contact between talus material and valley sediment fill (Figure 2). The gravel-surface parking lot caps a former landfill, the subject of a subsurface investigation (National Park Service, 2013) that allowed some verification of our geophysical interpretations.

METHODS

We used three near-surface geophysical methods to locate the basal contact of the talus deposit: GPR, SR, and 2DR. These techniques have been employed on talus slopes in the Swiss Alps, demonstrating the feasibility of geophysically imaging talus-bedrock contacts in some situations (Hoffmann and Schrott, 2003; Otto and Sass, 2006; and Sass, 2006, 2007). In addition to being non-invasive, under the right circumstances these techniques can offer rapid results and correlatable features between methods (Otto and Sass, 2006; Sass, 2006, 2007). We employed all three geophysical methods along the same survey line in order to compare results and refine the overall interpretation. Where possible, we validated our geophysics interpretation with borehole data from the landfill investigation. As a result of the protected status of Yosemite National Park, no other invasive subsurface investigation was permitted.

GPR Methods

We used the common offset method of GPR reflection surveying (Neal, 2004). An important assumption in GPR data presentation is that radar reflections originate from directly beneath the survey equipment. Corrections must be made for dipping reflectors or reflections from above-ground features (e.g., large boulders or trees). In this study, correction was made manually rather than by migration techniques (e.g., Porsani et al., 2006).

We conducted the GPR survey using a Sensors & Software pulseEKKO PRO unit with both 50-MHz and 100-MHz antennas in bistatic configuration. The lower frequency antenna provides deeper penetration (approximately 45–50 m) but lower (coarser) resolution, while the higher frequency antenna enhances resolution but reduces the maximum depth penetration (approximately 35–40 m) (Jol, 1995; Smith and Jol, 1995). Using both antennas allowed comparison and maximization of data quality at different depths. Transmitting and receiving antennas were set at 1 m apart (Sensors & Software, 1999a), with radar traces collected at 0.5-m intervals along the survey line. GPR data were acquired during late October, the driest part of the year, reducing the effect of near-surface attenuation by soil moisture.

We processed GPR data using Sensors & Software EKKO View Deluxe 4 software and applied basic processing methods, including DEWOW filtering and constant gain (Fisher et al., 1992; Sensors & Software,

Figure 3. Field images of the eastern margin of the studied talus deposit near Curry Village showing the location of geophysical survey line (red line): (A) Upper portion of talus slope near cliff face; (B) Traversing the small seasonal stream bed; (C) Gradual slope near boundary of talus against glacio-fluvial sediment fill; (D) Fluvial sediment from seasonal stream at distal edge of talus slope.

1999b). Using elevations from a 1-m LiDAR-derived digital elevation model (DEM), we applied a topographic correction to the GPR data, as there is significant relief along the survey line. We converted from travel time to depth using a velocity of 0.14 m/ns, an average for the expected material in the talus deposit (Otto and Sass, 2006), in which velocity in dry soil/dry sand = 0.15 m/ns and velocity through granite = 0.13 m/ns (Sensors & Software, 2006).

SR Methods

We conducted the SR survey using two 24-channel Geometrics Inc. Geode model seismographs and 48 geophones at variable spacing along the survey line. We used 3-m spacing for the southern portion (closer to the cliff face), where the talus was thought to be relatively thinner, and 5-m spacing for the northern portion (closer to the valley floor), resulting in a total line length of 200 m. Offset shots added another 40 m to this survey line length. Seismic energy was derived from gunpowder blasts triggered with a modified Betsy Seisgun™. We fired shots at 21 sites along the geophone array as well as at offset locations out from the northern end of the profile line toward the center of Yosemite Valley. Shots were detonated at 0.5–1 m depth in hand-augered backfilled holes. Offset shots were not possible on the south end of the survey line because of the steep bedrock cliff south of the apex of the talus slope. Four to eight stacked shot traces at each geophone for each shot point enhanced the desired signal and reduced non-coherent noise (e.g., automobile traffic, footfalls of hikers, wind, etc.). The SR survey was completed during late spring and summer, when ground conditions were relatively dry and the water table was expected to be at a low level.

We conducted a separate seismic velocity experiment on site bedrock in order to independently measure the P-wave velocity in this material. For this experiment we epoxied six metal disk geophone mounts directly to the bedrock face and used sledgehammer strikes on the bedrock face as the seismic energy source.

We analyzed the seismic refraction data using the Geometrics Inc. SeisImager/2D™ software package, which includes the PickWin™ and PlotRefa™ modules. We hand-picked first arrivals from each raw stacked geophone trace. This information was converted into travel time curves for each shot location along the survey line and was later combined into a single data file. To calculate the depth of potential refractor(s), we applied three methods: time-term inversion, network-raytracing, and tomography. Surface topography was incorporated using elevations from the 1-m LiDAR-derived DEM. Producing a tomographic inversion was particularly important for this study because (1) lateral variations in seismic velocities are expected within the talus deposit as a result of locally variable densities, and (2) the steeply dipping talus-bedrock contact is an expected and critical feature of interest to the study. We iterated the tomographic inversion twice, per Geometrics' recommendation, and applied network-raytracing to assess the misfit between the final model and the original data (Geometrics, 2006).

2DR Methods

Electrical resistivity values are highly affected by several variables, including lithology, the presence of water and/or ice, the amount and distribution of pore space in the material, and temperature (Reynolds, 1997). The expected resistivity for granite is approximately 300–3,000,000 Ω-m, while talus is expected to produce a range of values between 100 and 5,000 Ω-m, and valley fill is expected to range from 10 to 1,000 Ω-m (Loke, 2000; Sass, 2007). The presence of moisture or groundwater reduces resistivity values compared to dry values, resulting in the large ranges for any given material. Given these variations of many orders of magnitude, the contacts between talus and crystalline bedrock or glacio-fluvial valley fill can potentially be identified on the basis of large contrasts in resistivity values.

We acquired 2DR data using an Advanced Geosciences, Inc., SuperStingR1™ resistivity IP/SP system. The resistivity array consisted of a 28-electrode passive cable spaced at 6-m intervals and connected to stainless-steel electrode stakes. The resulting profile length of 168 m was moved in a 50 percent roll-along–type array to maximize linear coverage. To ensure proper electrical coupling with the ground, the soil around each electrode stake was wetted with salt water. Current was applied to the subsurface using a dipole-dipole roll-along survey. We increased the sampling detail along the upper end of the profile by increasing the number of unique dipole-dipole pairs, as imaging the interface of talus against crystalline bedrock and glacio-fluvial valley fill was a primary objective of the study. The SuperstingR1 handled the following tasks: auto-ranging of current and voltage to maximize signal levels, data stacking with standard deviation, and automatic switching of all electrode geometries with the switchbox28 system.

We analyzed the 2D-resistivity data using Advanced Geosciences, Inc. EarthImager 2D Resistivity and IP Inversion software. This program solves for the best-fitting smooth model solution from surficial apparent resistivity data. Topographic corrections obtained from the LiDAR-derived DEM were applied to the electrode positions to increase the accuracy of the final model. Resistivity modeling begins with an initial model based on the average raw data value, followed by iterative forward and inverse modeling. During these iterations, the software compares the resulting synthetic data from a forward model to the measured results and iteratively varies the inverse model resistivity values to decrease the misfit between the model result and the measured data. If model convergence is not achieved by a root mean square (RMS) error of less than 10% percent and L2 close to 1, then a small amount of misfit raw data is removed (<5 percent of the total) and the model is started over (Advanced Geosciences, Inc., 2013).

RESULTS

GPR Results

Evaluation of the 50-MHz and 100-MHz GPR data revealed numerous radar reflectors beneath the talus surface (Figure 4). A pair of features at the south end of the profile (between position 0 and 45 m along the profile at times 0 to 1,100 ns) dip steeply toward the valley. This is clearly evident in the 50-MHz results and less so in the 100-MHz data. We interpret the pair of features to be the bedrock-talus contact and a sheeting joint parallel to that about 5 m beneath it. However, it is critical to evaluate whether these signals could be spurious: the result of the radar wave bouncing off the cliff face either through an airwave or a direct ground surface wave. In other words, the processing software assumes that all energy returning from a radar pulse originates from reflections directly underfoot, even though returns could originate from anywhere in a shell of equal

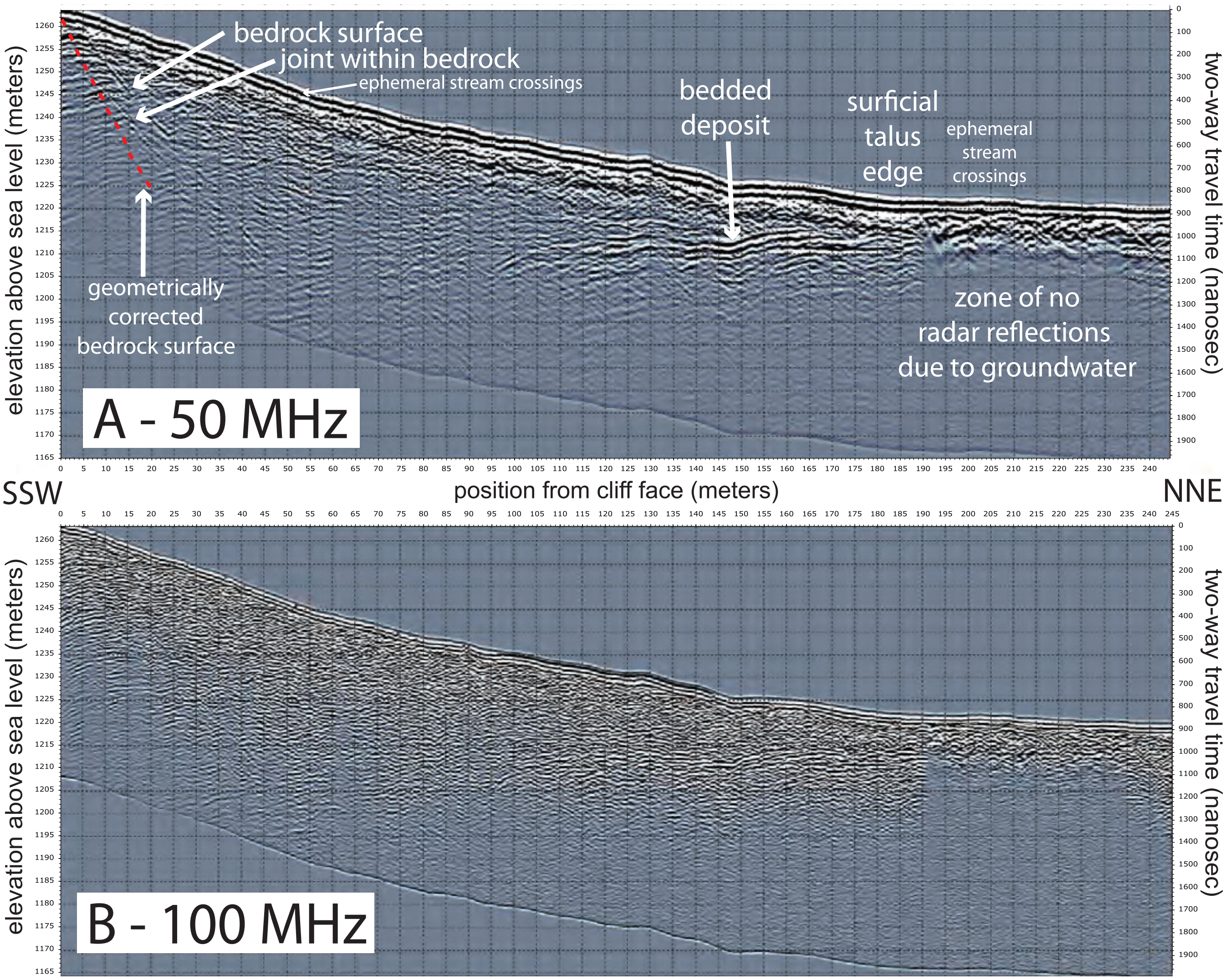

Figure 4. GPR data corrected for surface elevation, DEWOW filtered, using constant gain and a radar velocity of 0.140 m/ns. (A) 50-MHz results. (B) 100-MHz results. Note that steeply dipping reflectors, such as the bedrock contact with talus, must be geometrically corrected (see Figure 5).

travel time around the GPR apparatus. In order to test these alternate interpretations, we performed a simple velocity calculation to determine whether the reflector could have resulted from an airwave or direct ground wave using the equation $D = v \times T/2$, where D is the one-way distance to the reflector, v is velocity, and T is two-way travel time. From this calculation, it is evident that the signal is not the result of an airwave bouncing off surface bedrock at the south end of the profile, since the resulting velocity (0.08–0.1 m/ns) is much slower than that of a radar wave through air (0.3 m/ns). The same logic makes a refracted airwave unlikely. The interpretation that the signal is the result of a ground wave bouncing off surface bedrock at the south end of the profile is permissible based on the range of possible surface soil velocities, but this is unlikely for two reasons. First, the ground wave explanation cannot easily account for the parallel reflectors. Second, the radar wave velocity needed to explain this as a ground wave is somewhat slower than recommended values (Sass and Wollny, 2001; Otto and Sass, 2006; Sass, 2006, 2007; and Sensors & Software, 2006) for dry porous material such as the talus on the profile line surface at the time of the survey. Furthermore, previous studies have succeeded in locating bedrock-talus contacts and joints within bedrock, demonstrating the feasibility of imaging such structures (e.g., Toshioka et al., 1995; Sass and Wollny, 2001; Porsani et al., 2006; and Sass, 2006).

Since the steeply dipping reflectors at the south end of the GPR profile appear to be real, with the upper one corresponding to the inferred bedrock-talus interface, a geometric correction is required in order

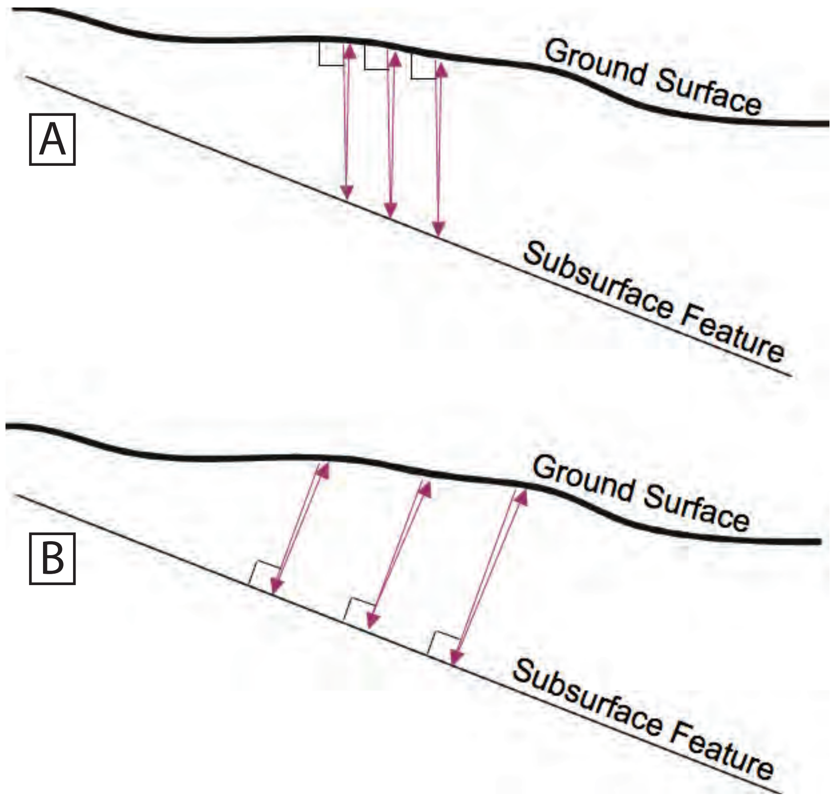

Figure 5. GPR dipping reflector correction. (A) All reflected energy is initially assumed to return from directly beneath the GPR, regardless of reflector dip. (B) Geometric correction for dipping reflectors stems from the fact that angle of incidence equals angle of reflection. A non-directional radar pulse will return significant reflected energy perpendicularly from the dipping structure rather than from the same dipping reflector directly beneath the instrument.

to render its true orientation. This correction is based on the fact that a radar wave is emitted as a non-directional pulse, but the GPR records the signal as if it derived from returns perpendicular to the ground surface. Since a strong signal, such as that in the 50-MHz results, would be expected if the radar wave had been reflected off a subsurface feature perpendicular to the angle of incidence (Figure 5), we calculated the true orientation of the dipping reflector along the southern end of the profile (from position 0–20 m). This correction yields a true dip of the talus-bedrock interface between 52° and 64° from horizontal, consistent with field measurements of the dip angle of the bedrock cliff adjacent to the apex of the talus slope.

There are also multiple, parallel, strong reflections within the middle portion of the profile (between position 110 and 170 m along the profile at travel times of 1,100–1,200 ns and calculated subsurface elevations of 1,210–1,218 m), which appear to shallow toward the north. This component of the data could represent the onlap of talus over glacio-fluvial sediment fill (Figure 6). As previously stated, we assume that after deglaciation ca. 15 to 17 ka, the valley floor was relatively flat bottomed. As talus accumulated, the deposit should have prograded northward into the valley, synchronous with aggradation of the valley floor with glacio-fluvial sediment; this would result in a contact between talus and fill that dips toward the cliff (Figure 6). The multiple, apparently bedded reflectors are either bedded sediment fill with talus deposited on top or coarse bedding within the lower portion of the talus deposit (Figure 5). The magnitude of the dip of this feature is a function of the radar wave velocity chosen but in this case is consistent with other geophysical data. These alternative interpretations and the dip of these reflectors are further developed in the Discussion section.

In addition, the GPR data reveal a zone lacking strong internal reflectors between 190 and 235 m along the profile line and beneath approximately 1,100-ns travel time (Figure 4) in both the 50-MHz and 100-MHz results. Since attenuation increases with increasing water content (Neal, 2004), such a feature could originate from attenuation by soil moisture or groundwater, but could alternately result from the presence of bedrock lacking internal structure (Sass, 2007). Numerous concave-down hyperbolas are also visible throughout the profile (e.g., between positions 135 and 140 m at time 900 ns),

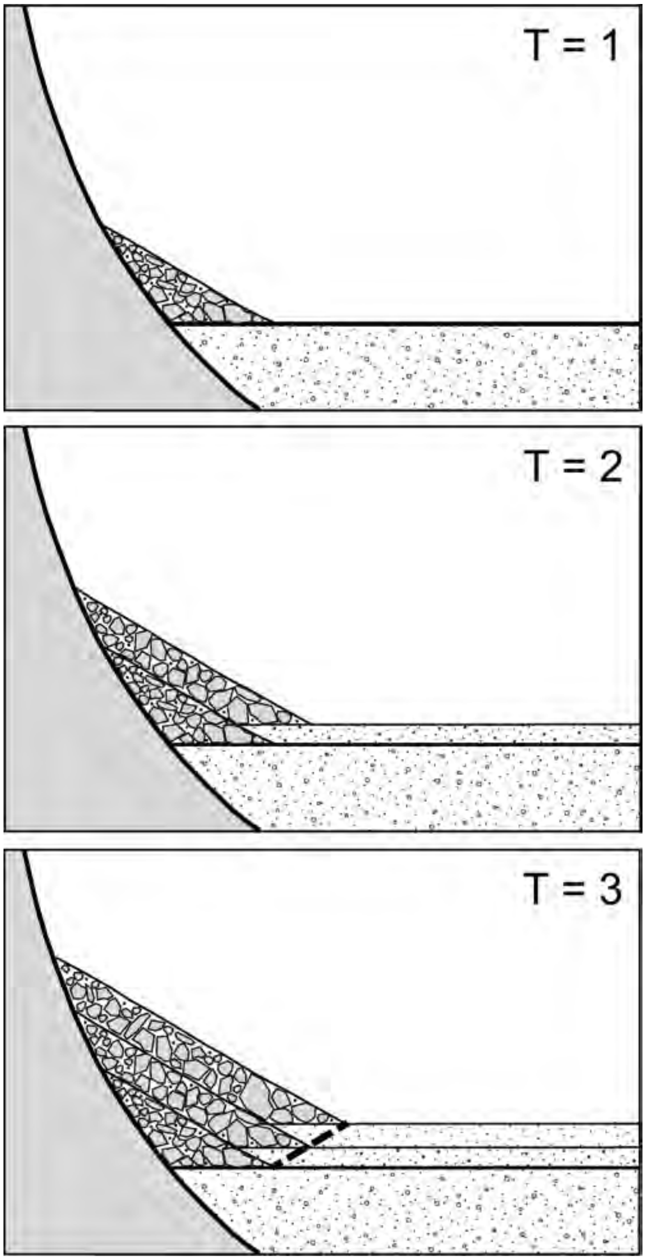

Figure 6. Schematic of post-glacial talus and glacio-fluvial deposition, showing distal edge of talus prograding out onto aggrading glacio-fluvial sediment fill. Steady deposition of both talus and glacio-fluvial sediment (shown here in three time snapshots) produces a "back dip" of the basal talus contact that dips toward the cliff.

which we interpret as internal reflections from large boulders within the talus.

SR Results

Tomographic modeling along the profile line (Figure 7B) generated 18 layers with seismic velocities ranging between 300 m/s at the surface to 5,000 m/s at depth. Examination of raypaths (Figure 7C) through the tomographic model provides information about the regions of accuracy of the model. The dense clustering of raypaths down to 30–40-m depths and away from the ends of the survey line demonstrates that the model is likely well constrained in these regions. At greater depths and at the survey line termini, the raypaths become increasingly diffuse, suggesting that the model is less well determined in these domains. Overall, the tomographic model is considered to be a good representation of the subsurface to a depth of 30–40 m in the middle and north end of the model along the profile line. Accuracy is compromised on the south end of the profile as a result of (1) the lack of offset shots on the southern end of the SR profile, (2) the absence of geophones directly on exposed bedrock, and/or (3) the probable steep dip of the bedrock-talus contact, which makes refracted seismic energy less likely to pass into bedrock and back to the surface in measurable amounts. Thus, the SR tomographic model does not represent the southern extreme end of the profile accurately in the area of greatest interest.

The SR tomographic model is consistent with published seismic velocities for different earth materials as well as with our own measurements of bedrock P-wave velocity. Seismic velocities for talus are expected to range from 100 to 4,600 m/s (Reynolds, 1997). The measured surface velocity of 387 m/s in the upper several meters of the profile line is consistent with materials such as dry unconsolidated soil and sand, as observed along the profile line surface during the survey. P-wave velocity values in the best-fit tomographic model increase with depth in most parts of the model to approximately 1,500–2,400 m/s. This is typical of materials such as floodplain alluvium and is in good agreement with the surficial velocity values from Gutenberg et al. (1956) across the middle of Yosemite Valley. At the subsurface south end of the profile, the SR tomographic model approaches an average velocity of 5,000 m/s, which is within the acceptable range for the velocity associated with granites (4,600–6,200 m/s; e.g., West, 1995), velocities on granite measured in Yosemite Valley (5,250 m/s: Gutenberg et al., 1956; 5,900 m/s: Zimmer et al., 2012), and values derived from our independent surficial bedrock seismic velocity survey at the study site (4,840–5,971 m/s).

Given published results and our observed seismic velocities, a talus-bedrock boundary would be identified in the seismic refraction data by the presence of a strong velocity gradient. This is the case because by its very nature, the tomographic model produces continuously varying velocities with no velocity discontinuities. Accordingly, we identified several

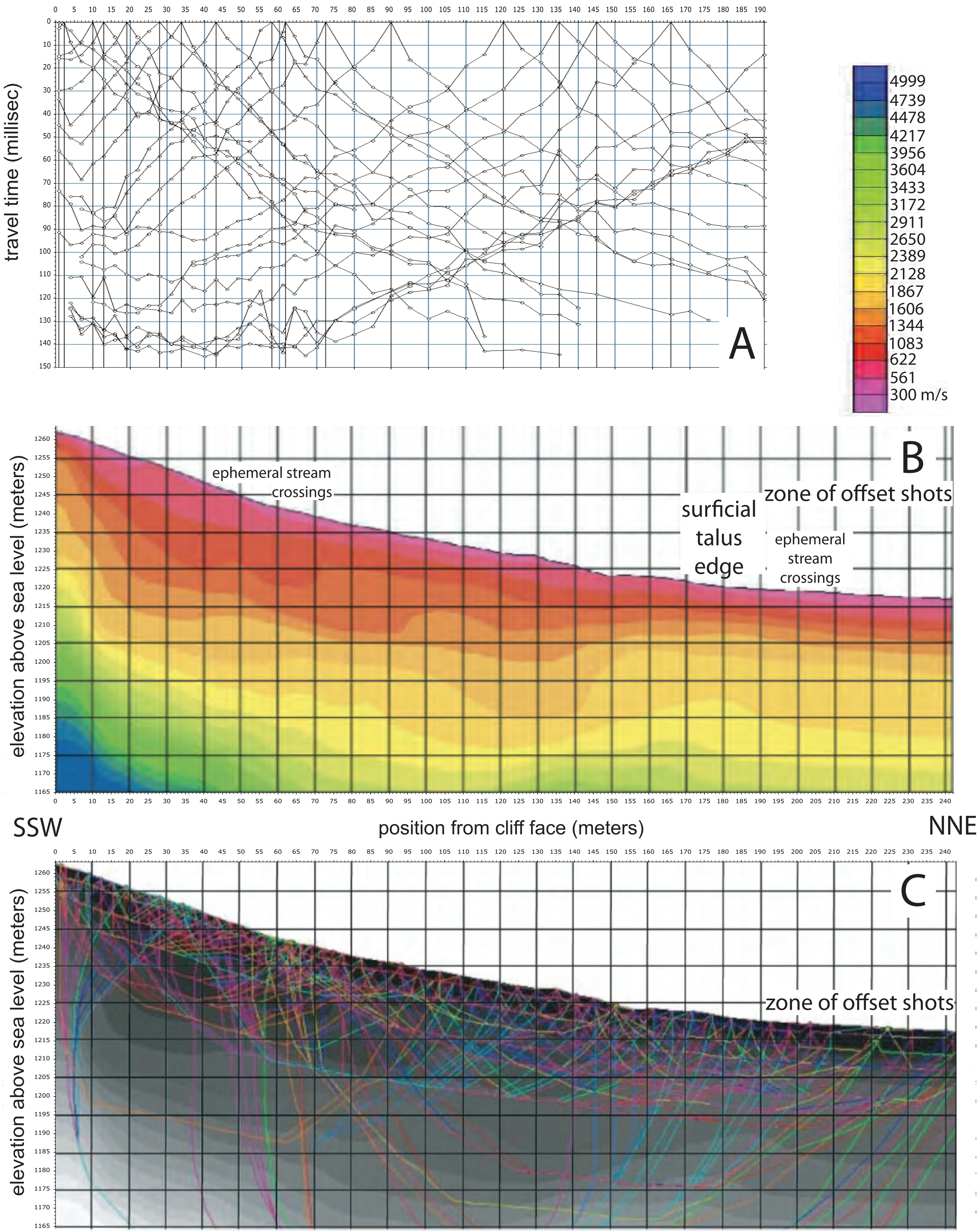

Figure 7. (A) Compiled travel time curves for seismic refraction survey line. (B) Color tomographic seismic refraction model. (C) Monochrome tomographic model with raypaths (colored lines).

features of the tomographic model. There is a strong velocity gradient (between 1,344 and 4,217 m/s) within the southern segment of the profile near the cliff face (between 0 and 40 m along the survey profile) that is of the approximate range to be a talus-bedrock boundary dipping steeply northward toward the valley. This gradient separates relatively high seismic velocities (4,478–4,999 m/s) of the magnitude of bedrock from lower velocities (1,344–2,911 m/s) of the magnitude of talus. Despite the stated accuracy problems in the tomographic model in this region, we consider it probable that this feature represents the talus-bedrock contact for two reasons. First, the surface location of the talus-bedrock contact at the top of the talus slope is known, and second, this strong velocity gradient dips 60° toward the valley, similar to the 60°–65° slope of the exposed cliff above the talus slope.

There is another strong seismic velocity gradient between 822 and 1,876 m/s present within the middle portion of the profile (between 120 and 160 m horizontal position along the profile). This feature appears to decrease in depth toward the north and then flattens out into the valley, similar to the prominent GPR reflectors in this region. The position at the ground surface and velocity difference across this feature are consistent with the interface between talus and glacio-fluvial sediment fill. This feature is corroborated by both of the other geophysical methods employed.

2DR Results

The RMS value indicates the amount of data misfit in the inverted resistivity section. While an RMS error value of <5 percent is ideal for processing, RMS values of <10 percent are deemed acceptable for these data, per the recommendation of Advanced Geosciences, Inc. (AGI). The overall RMS error for our 2DR model was 9.82 percent, while repeat measurement errors on individual data points were <2 percent in nearly all cases. Measured voltage values were >>1 mV in nearly all cases, while injected currents were fairly low at several mA. These indicators suggest that for this low-noise location survey results are robust, despite very high contact resistances of thousands of Ohms for the survey hardware.

Evaluation of the 2DR data reveals very strong variations in resistivity values along the profile (Figure 8A). At the surface of the southern end of the profile, resistivity values range in the tens of thousands to more than 100,000 Ω-m, while the near-surface section of the northern end of the profile range from <40 to a few thousand Ω-m. The most prominent feature in the 2DR is the nearly horizontal boundary along the 45–165-m section of the survey line, separating resistivity values in the tens or hundreds of thousands of Ω-m near the ground surface (red, orange, and yellow on Figure 8A) from values in the thousands of Ω-m below that (greens and yellows on Figure 8A). Although mainly horizontal, this resistivity boundary shallows northward toward the ground surface at 150–180 m along the survey profile.

The high resistivity values at the southern end of the survey profile (Figure 8A) are consistent with dry talus observed at the ground surface. There is no distinct talus-bedrock contact identified here in the 2DR, partly as a result of the impossibility of collecting surface data across the talus-bedrock boundary and partly because of the steep dip of the talus-bedrock contact. This boundary is simply not within the model space of the inversion. Consequently, the 2DR survey did not permit significant imaging of the talus-bedrock contact. The middle portion of the profile exhibits a wide variation in resistivity values, ranging from ~2,000 to ~6,000 Ω-m at depth to ~6,000 to >100,000 Ω-m near the surface. The lower values deeper in the profile are indicative of materials such as low-resistivity, moisture-retaining fines and clay, moist sand, and gravel up to intermediate-resistivity dry sand. The high values above this boundary are consistent with more-porous and drier higher-resistivity talus near the ground surface. The nearly horizontal boundary between medium and high resistivity values in the middle of the profile corresponds to the GPR reflectors in the same area (Figure 9A). Therefore, this strong contrast in resistivities is interpreted as the basal contact of talus against glacio-fluvial sediment fill. The low-resistivity (blue) region in the subsurface (Figures 8A and 9A) northern end of the 2DR profile could result from groundwater or moist fine-grained sediments.

DISCUSSION

In previous studies that imaged talus-bedrock contacts using GPR (Sass and Wollny, 2001; Otto and Sass, 2006; and Sass, 2006, 2007), two different approaches were used to locate the boundary. In some locations marked contrasts in dielectric constant between bedrock and talus produce distinct GPR reflections (e.g., Sass, 2006). In other cases, these materials have similar dielectric constants, such that the bedrock surface is noticeable as a boundary between talus showing distinct internal reflectors and bedrock that does not (e.g., Sass, 2007). Which of the cases will be displayed is dependent upon whether the bedrock is massive, without extensive jointing or

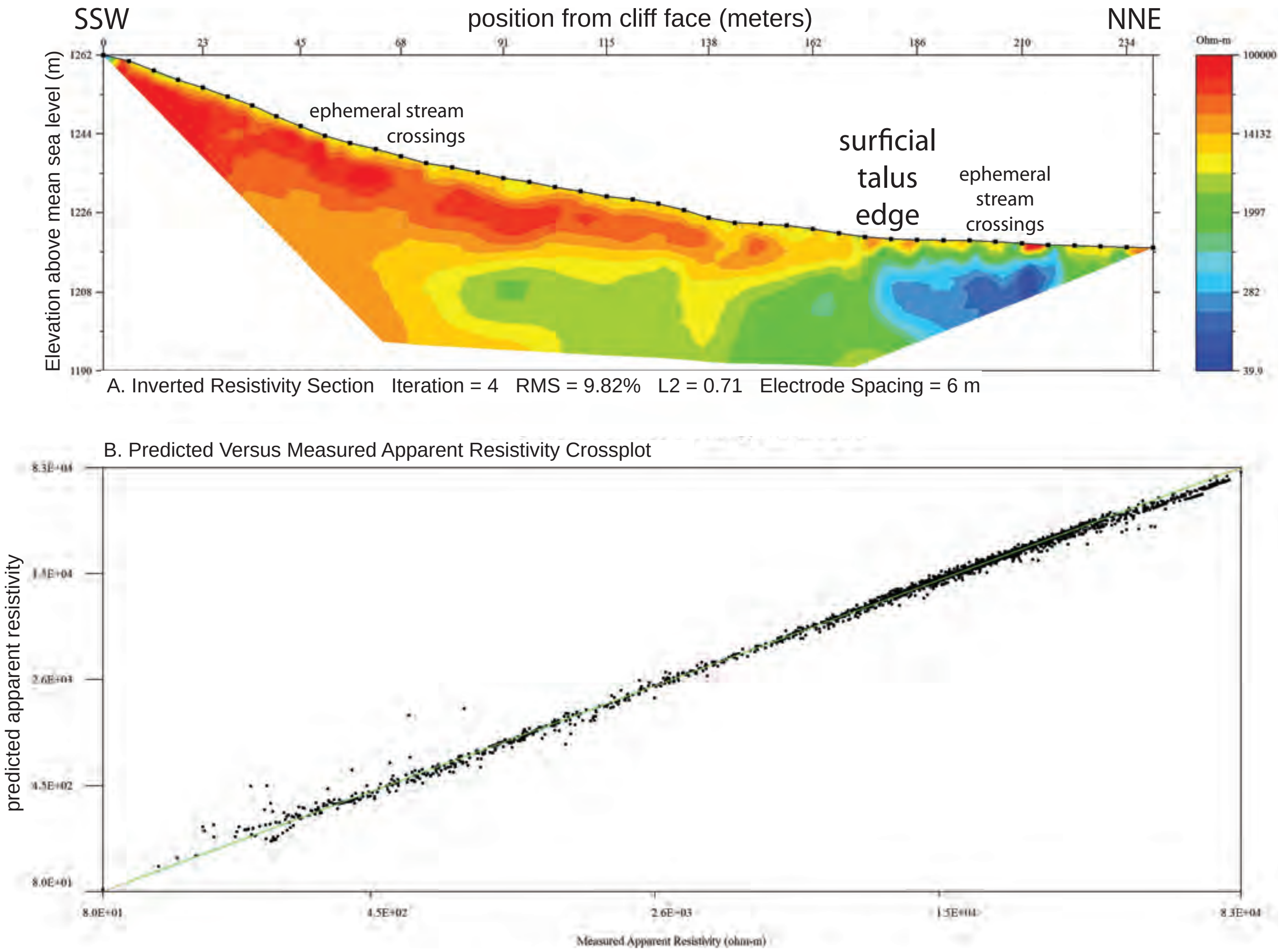

Figure 8. 2DR results. (A) Inverted resistivity section. (B) Cross plot of predicted versus measured apparent resistivities.

bedding, and whether there is a marked contrast in dielectric properties of the two contacting materials.

Our data exhibit a bedrock surface showing a clear GPR reflection, but they equivocally display a bedrock surface marked by a lack of internal GPR reflections. The uppermost steeply north-dipping distinguishable reflector on the south end of the GPR survey (closest to the cliff face) is interpreted to be the basal contact of talus against crystalline bedrock (between positions 0 and 45 m at travel times of 0–1,100 ns). Furthermore, an additional, parallel reflector is interpreted to be a surface parallel sheeting joint, which is a common feature on the Glacier Point Apron. Fractures and joints in bedrock have been successfully imaged in multiple studies (Toshioka et al., 1995; Sass and Wollny, 2001; Porsani et al., 2006; and Sass, 2006). The dip of the corrected GPR feature (52°–64° from horizontal) is similar to the local cliff angle, which supports the idea of a bedrock reflector. This reflector is clearly not an airwave reflecting off of the cliff face, and a ground wave bouncing off of the cliff face is also unlikely, since there are two parallel reflectors evident in the GPR at this location. On the other hand, the lack of GPR reflectors along profile line positions 190–235 m and >10 m in depth is consistent with Sass's (2007) method for identifying bedrock. However, this zone could instead signify strong GPR attenuation due to groundwater, clayey lithologies, etc. Correspondence of multiple geophysical methods is necessary for accurate interpretation in this region and will be discussed below.

The series of GPR reflectors evident in the middle portion of the profile (between positions 110 and 170 m) probably signifies the boundary of talus with glacio-fluvial sediment fill. However, it is uncertain whether the top or bottom of this series of reflectors represents the base of talus. Previous work (Otto and Sass, 2006; Sass, 2006, 2007) demonstrates the presence of internal reflectors in both rock-fall talus and debris avalanche deposits. Additional uncertainty stems from the apparent southward dip of the

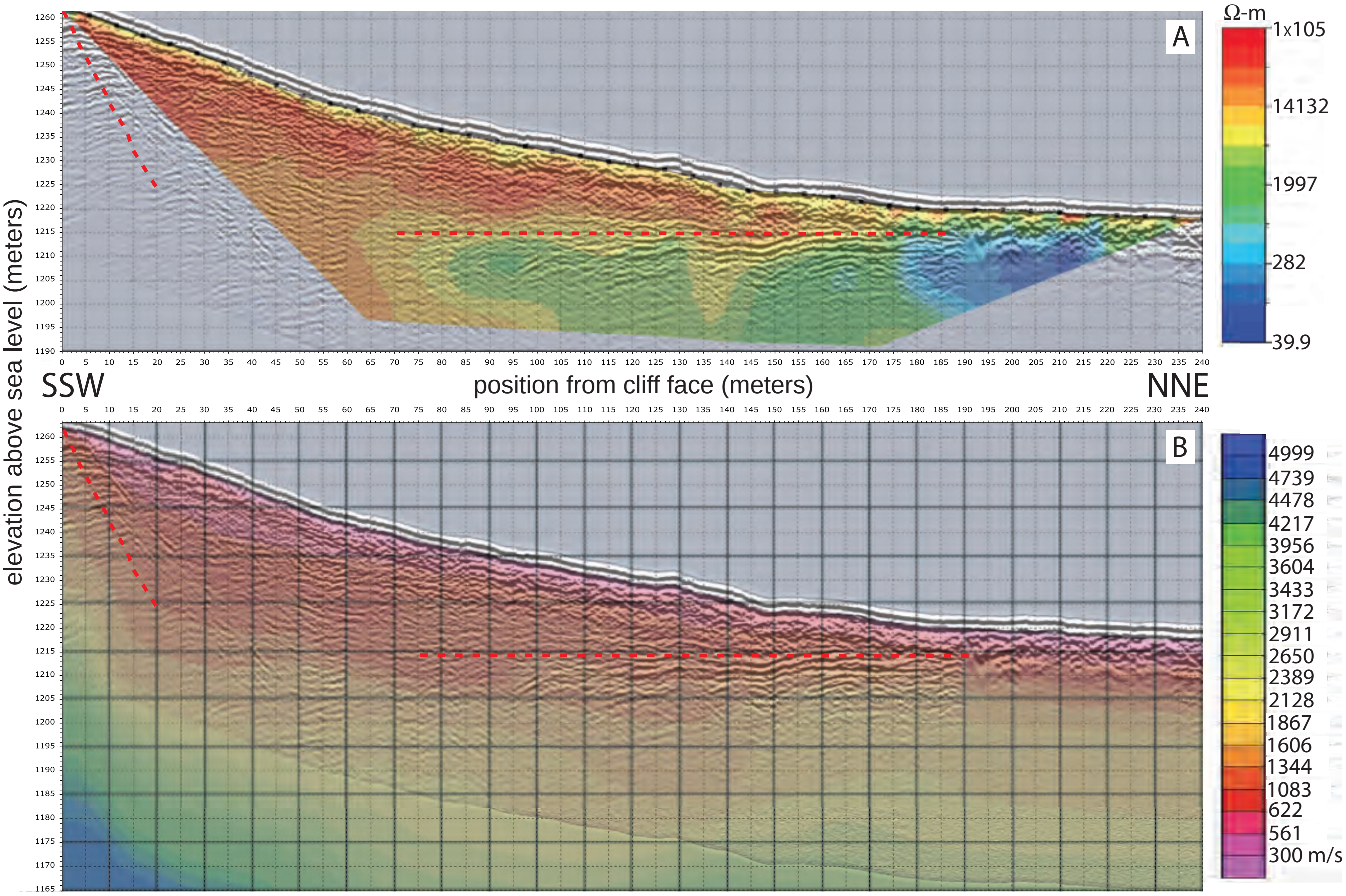

Figure 9. Geophysical data overlays. In both figures, the red dotted line represents the corrected position of the bedrock-talus contact and the glaciofluvial valley fill-talus contact, identified from GPR. See text for further explanation. (A) 2DR overlay on 50-MHz GPR. (B) Seismic refraction tomographic inversion overlay on 50-MHz GPR.

reflectors. This could be explained by the progressive onlap of rock-fall debris onto aggrading post-glacial fluvial deposits in the valley (Figure 6) or an inaccurate choice for the local radar wave velocity for this part of the profile. At locations 175–190 m along the profile, the talus deposit ends and there is indication of ~5 m of aggradation (Figure 4). This talus apron edge in the GPR is consistent with that identified in the high-resolution LiDAR-derived DEM. Elsewhere in Yosemite Valley, there is evidence of approximately 5 to 7 m of aggradation since deglaciation (Cordes et al., 2013), rendering these results mutually supportive.

As previously stated, limitations of the SR profile geometry reduced the ability to accurately image the southern end of the profile. This explains the absence in the SR model of known 5,000+ m/s bedrock at the surficial extreme southern end of the profile. Despite this, the SR survey provided subsurface constraints on the basal contact of talus against crystalline bedrock. Our data suggest that the strong, steeply dipping, seismic velocity gradient in the southern portion of the profile line closest to the cliff face, ranging from 1,344 to 4,217 m/s, likely represents this boundary.

Another important feature of the SR tomographic model is the presence of low-velocity material thinning northward toward the valley. The velocities of this triangular-shaped body (in cross section) are consistent with talus. If the lower boundary of this body is taken to be 1,342–1,724 m/s then it corresponds to the strong, stratified GPR reflectors at profile line positions 130–190 m and depths around 5–10 m. Here, the feature appears to ramp up northward toward the ground surface. The edge of the talus deposit at the ground surface is known to be at profile position ~175 m. Therefore, it can be inferred that low-velocity talus material to the south indistinguishably grades directly into surficial, unconsolidated, post-glacial, fluvial sediment fill to the north along the profile line (Figure 9A). Overall, the interpretations of these prominent features in the tomographic model suggest a triangular-shaped body of the main talus deposit (Figure 7).

The 2DR survey (Figure 8) yielded results that are broadly consistent with those of the other geophysical methods. In the Swiss Alps, Sass (2007) determined the location of bedrock based on the presence of a strong electrical contrast between the talus material and the bedrock. In addition, he suggested that it is impossible to assign a resistivity value to the bedrock interface because of the smooth contrasts and variation in resistivity of the bedrock itself. Therefore, it can be difficult to identify the bedrock-talus interface based on 2DR data alone. Within the inverted resistivity section, there are few indications of the basal contact of talus at the southern end of the section, and the bedrock-talus contact likely lies outside the inversion model space.

Interpretation Based on Multiple Geophysical Data Sets

The subsurface elevation of the basal contact of talus against crystalline bedrock or glacio-fluvial sediment fill was obtained from comparison of the GPR, SR, and 2DR processed data (Figure 9). Overlaying the SR or 2DR sections at 50 percent transparency on top of the 50-MHz GPR section highlights similarities in the results, leading to a high confidence in the processed geophysical data. In the combined SR-GPR image (Figure 9B) the SR velocity gradient along the southern end of the profile (closest to the cliff face) roughly corresponds to the corrected dipping reflector in the GPR section. In addition, strong correlation is also evident farther north along the survey profile line into the valley (profile position 120–185 m), where there is a southward dip of the pronounced velocity gradient in the SR model and similarly trending reflectors in the GPR section (Figure 9B). In the 2DR-GPR overlay (Figure 9A), interpretation of the basal contact of talus with crystalline bedrock is difficult, since the location of the corrected dipping GPR reflector falls outside the zone of 2DR coverage. However, striking similarities are apparent between the 2DR and GPR results further north along the profile line toward the valley (Figure 9A). Here, the orange-green boundary in the resistivity model correlates very well with the GPR reflectors, though it does not dip southward as clearly. The difference in dip of the feature could result from GPR imaging lithologic features, while resistivity revealed groundwater/moisture contrasts. Alternatively, this difference may arise from the user choice of radar wave velocity, but since the SR agreed well with the GPR, it is difficult to ascribe the difference to GPR processing choices alone. The north end of the survey line (profile positions 190–235 m) shows a strong correspondence between low resistivity (blue color) and the zone of no internal GPR reflectors (~10 m below grade). A nearby borehole and groundwater investigation conducted in May 2012 (National Park Service, 2013) indicates that the groundwater table was located at about 1,206–1,208 m in elevation in the region around profile positions 190–240 m. This elevation is very similar to that of the featureless zone in the GPR imaged during October 2009, making radar wave attenuation a likely explanation for the GPR. Similarly, the low resistivity in the same part of the profile is readily explained by the presence of groundwater. If the GPR attenuation and low resistivity are ascribed to groundwater, this would imply relatively similar groundwater elevations at the times of data collection. This feature is absent from the SR tomography model because there were no geophones in the region of offset shots at 200–240 m along the profile line. As a result, any anomalous velocities in this region would be smeared out along raypaths further southward into the tomographic model. The former landfill lies upgradient of the low-resistivity GPR-attenuation zone. Sampling results in the vicinity indicate no unusual solutes in the groundwater (National Park Service, 2013), excluding the landfill as a possible source for observed features in this part of the geophysical profile. In short, the GPR attenuation and low-resistivity zone is readily explained by groundwater.

Based on our geophysical data, the best interpretation of the overall talus geometry is that it reaches a maximum of ~40 m in thickness at about 50–80 m from the bedrock face at the south end of the survey line (Figure 9). The talus pinches out against bedrock at the south end of the survey line in the GPR data, in accordance with surface observations. The northward termination of talus at about 180 m along the survey line is evident at the ground surface and is consistent with the geophysical data sets (Figure 9). The 2DR shows this northward pinchout especially well (Figure 9A). Boreholes in the region north of the interpreted distal extent of talus encounter primarily glacio-fluvial sediment fill with only occasional large boulders, consistent with "outlier" boulders that are commonly observed beyond the edge of the active talus slope (Evans and Hungr, 1993). The apparent bedding in the GPR at survey locations 120–185 m likely results from either bedded glacio-fluvial sediment fill or coarse bedding in talus, but we cannot easily explain the southward dip if it is sediment fill. Alternatively, the apparent bedding in the GPR results could be restored to near horizontal with a different (slower) choice of radar velocity. However, this would also shallow the structure in general and would no longer agree with the boundaries also seen within the SR and 2DR, making this alternative less appealing. Thus, we prefer the hypothesis that growth of the talus cone occurred simultaneously with aggradation of glacio-fluvial sediment fill, creating a south-dipping contact between sediment fill and talus.

Optimization of Geophysical Surveys on Talus

GPR

GPR provided the most detailed subsurface information and was simplest to use in terms of field data acquisition and processing. Dry ground conditions at the time of the survey minimized radar attenuation, thereby optimizing our results. As was the case with other studies on talus (Sass and Wollny, 2001; Otto and Sass, 2006; and Sass, 2006, 2007), GPR provided good penetration depth and resolution of subsurface structures, allowing for a detailed interpretation. Multiple crossing GPR lines may have further improved the confidence of our interpretation, and we suggest this for future geophysical surveys on talus.

One potential source of error is the requirement to choose an average radar velocity to convert from travel time to depth. Despite likely velocity variations throughout the talus deposit, an average velocity (representative of the various materials present) was applied to the processing as a result of the limitations of the processing software and available velocity structure information.

SR

The SR survey proved to be the most challenging and least diagnostic of the three geophysical methods. There were limited areas suitable for augering holes for Betsy Seisgun™ shot locations and significant physical restrictions in terms of the geometry of the SR survey. As a result of the location of the profile line against the bedrock cliff face, offset shots were not possible on the southern end of the SR survey. Imaging of the talus-bedrock interface without any shots or geophones on the bedrock side of this contact severely limited SR imaging of this interface. At a minimum, future work of this type should consider including geophones epoxied to the bedrock cliff face in order to constrain the cliff face boundary position and its high seismic velocity. Another shortcoming of the geometry of this survey resulted from the difficulty in achieving the angle of critical refraction with shots close to the cliff face. For seismic waves to be refracted, raypaths must approach the refracting boundary at an angle such that energy is refracted along the boundary. Thus, distant shots were required to achieve significant refracted energy, but this energy attenuates with distance. For all of these reasons, it was technically challenging to image the bedrock-talus interface at depth at the south end of the survey line using SR.

Another limitation of the SR result stemmed from processing software limitations. The SR processing software is designed for relatively simple layered geology, so that default tomographic models have their lowest velocity at all points at the ground surface and highest velocity at the maximum depth of the model. It was not possible to specify known seismic velocities as boundary conditions before tomographic inversion, such as our ~6,000-m/s bedrock, at the south end of the profile at the ground surface as well as at depth all along the southern end.

2DR

The 2DR survey was the most rapid of the three geophysical methods. The electrodes were easy to position in the ground, but high contact resistances in this type of formation tended to reduce data quality. The necessity to wet each electrode location with salt water was somewhat cumbersome in this terrain. The possibility of imaging the bedrock-talus contact at depth was prevented by the steep dip of the contact and the inability to set the 2DR survey across the surface expression of the bedrock-talus boundary. On the other hand, the 2DR result provided excellent corroboration with GPR imaging of the talus-sediment fill contact. This suggests that combining 2DR and GPR may be ideal for geophysical surveying in deposits and geometries similar to this study area.

CONCLUSIONS

This study applied near-surface geophysical methods to map the extent of subsurface talus in a region of active accumulation by rock fall. These data are helpful for quantifying the total volume of talus beneath Glacier Point, to supplement the historical record of rock falls, and to put modern process rates into context (Brody, 2011), but the goal of this study was to evaluate the feasibility of using geophysics to map the subsurface in these materials. To constrain the basal contact of talus against crystalline bedrock or glacio-fluvial sediment fill, GPR, SR, and 2DR were used to define this interface. Of the three near-surface geophysical techniques utilized, GPR provided the most detailed image of the subsurface of the talus deposit (Figure 4). 2DR produced strong contrasts between talus and valley fill but could not resolve the talus-bedrock interface, as a result of its steep dip at the edge of the survey line. The physical geometry of rock-fall–generated talus cones is not amenable to the best practices of SR surveys. The lack of offset shots in the region of greatest interest—near the talus-bedrock contact—strongly limits SR applicability in some regions. Nonetheless, there were strong congruencies among the SR, GPR, and 2DR data.

Overlaying the SR or 2DR results over the GPR section strengthened the interpretation of a basal contact of talus against crystalline bedrock and glacio-fluvial valley fill, with a maximum deposit thickness of approximately 45 m (Figure 9). At the survey line location, the bedrock-talus contact dips at about the same angle as the Glacier Point Apron surface. The contact between talus and glacio-fluvial sediment fill seems to dip southward, suggesting an onlapping relationship with sediment fill as the valley floor aggraded about 5 m after deglaciation (Figure 6). The surface location of the edge of talus agrees with the predicted location from the geophysics. The results of this study suggest that GPR and 2DR may be sufficient to accurately image subsurface contacts in geologic materials such as these.

ACKNOWLEDGMENTS

We gratefully acknowledge Horacio Ferriz (California State University, Stanislaus), Greg Johnston (Sensors & Software, Inc.), Craig Lippus (Geometrics, Inc.), and Brad Carr (Advanced GeoSciences, Inc.) for technical advice and assistance. Horacio Ferriz also graciously provided the GPR and resistivity equipment. Chad Carlson, Joey Luce, Preston Ward, Wayne Nick, and Dustin Smith assisted with field work. Andy Shriver and Robin Trayler assisted with GIS and figure preparation, respectively. Jerry DeGraff and John Wakabayashi provided valuable project advisement and review of early manuscript drafts, and the final manuscript benefited from valuable input from three anonymous reviewers. This research would not have been possible without grants from the California State University, Fresno College of Science and Mathematics (Faculty-Sponsored Student Research Grant), the Association of Environmental and Engineering Geologists (Sacramento Section student research grant and Norman R. Tilford Field Studies Scholarship), the Geological Society of America (Roy J. Shlemon Scholarship), and the Northern California Geological Society (Richard Chambers Memorial Scholarship).

REFERENCES

Advanced Geosciences, Inc., 2013, *Instruction Manual for EarthImager 2D Version 2.1.7 Resistivity and IP Inversion Software*: Geometrics, Inc. Austin, TX.

Bateman, P. C., 1992, *Plutonism in the Central Part of the Sierra Nevada Batholith, California*: U.S. Geological Survey Professional Paper 1483, 186 p.

Brody, A. G., 2011, *Quantifying Post-Glacial Talus Deposition in Yosemite Valley Using ARCGIS and Near-Surface Geophysics, and the Implications on Hazard Assessment*: M.S. Thesis, California State University, Fresno, 169 p.

Bronson, B. R. and Watters, R. J., 1987, The effects of long-term slope deformations on the stability of granitic rocks of the Sierra Nevada, Nevada, California. In *Proceedings of the 23rd Engineering Geology and Soils Engineering Symposium*: Utah State University, Logan, UT, pp. 203–217.

Bursik, M. I. and Gillespie, A. R., 1993, Late Pleistocene glaciation of Mono Basin, California: *Quaternary Research*, Vol. 39, pp. 24–35.

Cordes, S. E.; Stock, G. M.; Schwab, B. E.; and Glazner, A. F., 2013, Supporting evidence for a 9.6 ± 1 ka rock fall originating from Glacier Point in Yosemite Valley, California: *Environmental Engineering Geoscience*, Vol. 19, pp. 345–361.

Dussauge, C.; Grasso, J.-R.; and Helmstetter, A., 2003, Statistical analysis of rockfall volume distributions: Implications for rockfall dynamics: *Journal Geophysical Research*, Vol. 108, pp. 2–1–2-11.

Dussauge-Peisser, C.; Helmstetter, A.; Grasso, J.-R.; Hantz, D.; Desvarreux, P.; Jeannin, M.; and Giraud, A., 2002, Probabilistic approach to rock fall hazard assessment: Potential of historical data analysis: *Natural Hazards Earth System Sciences*, Vol. 2, pp. 15–26.

Evans, S. G. and Hungr, O., 1993, The assessment of rockfall hazard at the base of talus slopes: *Canadian Geotechnical Journal*, Vol. 30, pp. 620–636.

Fisher, S. C.; Stewart, R. R.; and Jol, H. M., 1992, Processing ground penetrating radar (GPR) data: *GPR Processing CREWES Research Report*, Vol. 4, pp. 11-1–11-22.

Geometrics, 2006. *SeisImager/2D Manual Version 3.2: Pickwin v. 3.2 and Plotrefa v. 2.8*: Advanced Geoseiences. Inc. San Jose, CA.

Gutenberg, B.; Buwalda, J. P.; and Sharp, R. P., 1956, Seismic explorations on the floor of Yosemite Valley, California: *Bulletin Geological Society America*, Vol. 87, pp. 1051–1078.

Guzzetti, F.; Reichenbach, P.; and Wieczorek, G. F., 2003, Rockfall hazard and risk assessment in the Yosemite Valley, California, USA: *Natural Hazards Earth System Sciences*, Vol. 3, pp. 491–503.

Hoffmann, T. and Schrott, L., 2003, Determining sediment thickness of talus slopes and valley fill deposits using seismic refraction—a comparison of 2D interpretation tools: *Zeitschrift Geomorphologie N.F. Supplement*, Vol. 132, pp. 71–87.

Huber, N. K., 1981, *Amount and Timing of Late Cenozoic Uplift and Tilt of the Central Sierra Nevada, California—Evidence from the Upper San Joaquin River Basin*: U.S. Geological Survey Professional Paper 1197, 28 p.

Huber, N. K., 1987, *The Geologic Story of Yosemite National Park*: U.S. Geological Survey Bulletin 1595.

Jol, H. M., 1995, Ground penetrating radar antennae frequencies and transmitter powers compared for penetration depth, resolution and reflection continuity: *Geophysical Prospecting*, Vol. 43, pp. 693–709.

Loke, M. H., 2000, *Electrical Imaging Surveys for Environmental and Engineering Studies—A Practical Guide to 2D and 3D Surveys*: Unpublished Short Training Course Notes, Penang, Malaysia, Universiti Sains Malaysia, 61 p.

Matasci, B.; Carrea, D.; Jaboyedoff, M.; Pedrazzini, A.; Stock, G. M.; and Oppikofer, T., 2011, Structural characterization of rockfall sources in Yosemite Valley from remote sensing data: Toward more accurate susceptibility assessment: *Proceedings of the 14th Pan-American Conference on Soil Mechanics and Geotechnical Engineering Conference*: Toronto, Canada, October 2011.

Matthes, F. E., 1930, *Geologic History of the Yosemite Valley*: U.S. Geological Survey Professional Paper 160, 225 p.

National Park Service, 2013, *Curry Landfill Site Remedial Investigation/RCRA Facility Investigation (RI/RFI) Report*: Yosemite National Park, Yosemite, Ca, October 2013, 282 p.

Neal, A., 2004, Ground-penetrating radar and its use in sedimentology: Principles, problems and progress: *Earth Science Reviews*, Vol. 66, pp. 261–330.

Otto, J. C. and Sass, O., 2006, Comparing geophysical methods for talus slope investigations in the Turtman valley (Swiss Alps): *Geomorphology*, Vol. 76, pp. 257–272.

Peck, D. L., 2002, *Geologic Map of the Yosemite Quadrangle, Central Sierra Nevada, California*: U.S. Geological Survey Geologic Investigations Series Map I-2751, scale 1:62,500.

Phillips, F. M.; Zreda, M.; Plummer, M. A.; Elmore, D.; and Clark, D. H., 2009, Glacial geology and chronology of Bishop Creek and vicinity, eastern Sierra Nevada, California: *Geological Society America Bulletin*, Vol. 121, pp. 1013–1033.

Porsani, J. L.; Sauck, W. A.; and Junior, A. O. S., 2006, GPR for mapping fractures and as a guide for the extraction of ornamental granite from a quarry: A case study from southern Brazil: *Journal Applied Geophysics*, Vol. 58, pp. 177–187.

Reynolds, J. M., 1997, *An Introduction to Applied and Environmental Geophysics*: Wiley, New York, 796 pp.

Sass, O., 2006, Determination of the internal structure of alpine talus deposits using different geophysical methods (Lechtaler Alps, Austria): *Geomorphology*, Vol. 80, pp. 45–58.

Sass, O., 2007, Bedrock detection and talus thickness assessment in the European Alps using geophysical methods: *Journal Applied Geophysics*, Vol. 62, pp. 254–269.

Sass, O. and Wollny, K., 2001, Investigations regarding alpine talus slopes using ground-penetrating radar (GPR) in the Bavarian Alps, Germany: *Earth Surface Processes Landforms*, Vol. 26, pp. 1071–1086.

Sensors & Software, Inc., 1999a, *Ground Penetrating Radar Survey Design*: Mississauga, ON, Canada.

Sensors & Software, Inc., 1999b, *Practical Processing of GPR Data*: Mississauga, ON, Canada.

Sensors & Software, Inc., 2006, *pulseEKKO PRO User's Guide*: Mississauga, ON, Canada.

Smith, D. G. and Jol, H. M., 1995, Ground penetrating radar: Antenna frequencies and maximum probably depths of penetration in Quaternary sediments: *Applied Geophysics*, Vol. 33, pp. 93–100.

Smith, S. J. and Anderson, R. S., 1992, Late Wisconsin paleoecologic record from Swamp Lake, Yosemite National Park, California: *Quaternary Research*, Vol. 38, pp. 91–102.

Stock, G. M.; Bawden, G. W.; Green, J. K.; Hanson, E.; Downing, G.; Collins, B. D.; Bond, S.; and Leslar, M., 2011, High-resolution three-dimensional imaging and analysis of rock falls in Yosemite Valley, California: *Geosphere*, Vol. 7, pp. 573–581, doi:10.1130/GES00617.1.

Stock, G. M.; Collins, B. D.; Santaniello, D. J.; Zimmer, V. L.; Wieczorek, G. F.; and Snyder, J. B., 2013, *Historical Rock Falls in Yosemite National Park, California (1857–2011)*: U.S. Geological Survey Data Series 746, 17 p. and data files: http://pubs.usgs.gov/ds/746.

Stock, G. M. and Uhrhammer, R. A., 2010, Catastrophic rock avalanche 3600 years BP from El Capitan, Yosemite Valley, California: *Earth Surface Processes Landforms*, Vol. 35, pp. 941–951.

Toshioka, T.; Tsuchidaa, T.; and Sasahara, K., 1995, Application of GPR to detecting and mapping cracks in rock slopes: *Journal Applied Geophysics*, Vol. 33, pp. 119–124.

Wahrhaftig, C. and Birman, J. H., 1965, The Quaternary of the Pacific Mountain System in California. In Wright, H. E., Jr. and Frey, D. G. (Editors), *The Quaternary of the United States—A Review Volume for the 7th Congress of the International Association for Quaternary Research*: Princeton University Press, Princeton, NJ, pp. 299–340.

Wakabayashi, J. and Sawyer, T. L., 2001, Stream incision, tectonics, uplift, and evolution of topography of the Sierra Nevada, California: *Journal Geology*, Vol. 109, pp. 539–562.

West, T. R., 1995, *Geology Applied to Engineering*: Long Grove, IL, Waveland Press, 560 p.

Wieczorek, G.; Nishenko, S. P.; and Varnes, D. J., 1995, Analysis of rock falls in the Yosemite Valley, California. In Daemen, J. J. and Schultz, R. A. (Editors), *35th US Symposium on Rock Mechanics*: A. A. Balkema, Daemen, pp. 85–89.

Wieczorek, G. F. and Jäger, S., 1996, Triggering mechanisms and depositional rates of postglacial slope-movement processes in the Yosemite Valley, California: *Geomorphology*, Vol. 15, pp. 17–31.

Wieczorek, G. F.; Morrissey, M. M.; Iovine, G.; and Godt, J., 1999, *Rock-Fall Potential in the Yosemite Valley, California*: U.S. Geological Survey Open File Report 99-578.

Wieczorek, G. F. and Snyder, J. B., 1999, *Rock Falls from Glacier Point above Camp Curry, Yosemite National Park, California*: U.S. Geological Survey Open-File Report 99-385.

Wieczorek, G. F.; Snyder, J. B.; Waitt, R. B.; Morrissey, M. M.; Uhrhammer, R. A.; Harp, E. L.; Norris, R. D.; Bursik, M. I.; and Finewood, L. G., 2000, Unusual July 10, 1996 rock fall at Happy Isles, Yosemite National Park, California: *Geological Society America Bulletin*, Vol. 112, pp. 75–85.

Wieczorek, G. F.; Stock, G. M.; Reichenbach, P.; Snyder, J. B.; Borchers, J. W.; and Godt, J. W., 2008, Investigations and hazard assessment of the 2003 and 2007 Staircase Falls, rock falls, Yosemite National Park, California, USA: *Natural Hazards Earth System Sciences*, Vol. 8, pp. 421–432.

Zimmer, V. L.; Collins, B. D.; Stock, G. M.; and Sitar, N., 2012, Rock fall dynamics and deposition: An integrated analysis of the 2009 Ahwiyah Point rock fall, Yosemite National Park, USA: *Earth Surface Processes Landforms*, Vol. 37, pp. 680–691, doi:10.1002/esp.3206.